ELSEVIER

Contents lists available at ScienceDirect

Journal of Solid State Chemistry

journal homepage: www.elsevier.com/locate/jssc



Synthesis and stability of Sn(II)-containing perovskites: (Ba,Sn^{II})Hf^{IV}O₃ versus (Ba,Sn^{II})Sn^{IV}O₃



Eric A. Gabilondo ^a, Shaun O'Donnell ^a, Rachel Broughton ^b, Jacob L. Jones ^b, Paul A. Maggard ^{a,*}

- ^a Department of Chemistry, North Carolina State University, Raleigh, NC, 27695-8204, USA
- b Department of Materials Science and Engineering, North Carolina State University, Raleigh, NC, 27695-8204, USA

ARTICLE INFO

Keywords: Perovskite Metastable solids Flux synthesis Metal oxide

ABSTRACT

While Sn(II)-containing perovskite oxides have long drawn attention as Pb(II) substitutes in technologicallyrelevant dielectric materials, they are also highly thermodynamically unstable and potentially impossible to prepare. Investigations into the new flux-mediated syntheses of metastable Sn(II)-containing hafnate and stannate perovskites were aimed at understanding the key factors related to their synthesizability. The BaHfO₃ perovskite was reacted with SnClF from 250 to 350 $^{\circ}$ C for 12–72 h, yielding an unprecedented Sn(II) concentration on the Asite of up to ~ 70 mol%, i.e., $(Ba_{0.3}Sn_{0.7})HfO_3$ in high purity. Elemental mapping using EDS shows the Sn(II)cations diffuse gradually throughout the crystallites, with two reaction cycles needed to give a nearly homogeneous distribution. In contrast, similar reactions with BaSnO3 and as little as 10 mol% Sn(II) result in decom $position \ to \ SnO_{2}, and \ BaSnO_{3}. \ The \ (Ba_{1-x}Sn_{x})HfO_{3} \ compositions \ exhibit \ a \ primary \ cubic \ perovskite \ structure$ $(Pm\overline{3}m; \text{ for } x = 1/3, 1/2 \text{ and } 2/3)$ by powder X-ray diffraction (XRD) methods, with the Sn(II) cations substituted on the A-site. Total energy calculations show the thermodynamic instability versus the ground state (i.e., metastability) for $(Ba_{1-x}Sn_x)HfO_3$ increases with Sn(II) substitution, reaching a maximum of ~ 446 meV atom $^{-1}$ at ~ 70 mol% Sn(II). The decomposition pathway of (Ba_{1/3}Sn_{2/3})HfO₃ was probed by ex situ XRD as well as in situ electron microscopy methods. An onset of thermally-induced decomposition begins at \sim 350-400 °C to give the more stable oxides which are found to segregate out in surface layers. These results help to elucidate the factors underpinning the synthesizability of highly metastable Sn(II)-containing perovskites, which increases with their cohesive energy and with the absence of lower-energy polymorphs or other ground states that can be reached without significant ion diffusion.

1. Introduction

The preparation of advanced oxide materials is a scientific challenge that is important for many potential technological applications, such as for their electronic, magnetic, or thermal properties [1–5]. Many previous synthetic approaches have been utilized to address solid-state synthetic challenges, including lower-temperature 'Chimie Douce' approaches that enable better kinetic control over product formation. These include hydrothermal, sol-gel, ionic liquids, and molten salt synthetic techniques. The latter approach, also called the flux synthesis method, facilitates the low-temperature preparation of metastable oxides in many different chemical systems [6–8]. The effectiveness of this synthetic method arises from the capability to utilize kinetic barriers inherent to both ion diffusion and nucleation-driven pathways. Successful reaction pathways to metastable materials are discoverable by

* Corresponding author.

E-mail address: paul_maggard@ncsu.edu (P.A. Maggard).

utilizing sufficiently low temperatures for their formation and kinetic stabilization, such as through soft cation exchange or flux-mediated nucleation.

Metastable solids are exemplified in the synthetic pursuit of Sn(II)-based perovskite oxides [9]. These are of particular interest as alternatives to the isoelectronic Pb(II) analogues because of their enhanced properties and reduced toxicity. Several Pb(II)-containing perovskite oxides exhibit technologically-relevant properties, such as ferro- and piezoelectricity in commercial PbZr_{1-x}Ti_xO₃ (PZT) [10] or antiferroelectricity in PbHfO₃ [11]. Their detailed and in-depth structural origins have been under investigation for many decades. Their ferroic properties are currently understood as being largely influenced by the spontaneous polarization, which is induced by the stereoactive $6s^2$ configuration of the Pb(II) cation [11,12]. Unfortunately, the synthesis of analogous Sn(II)-containing oxides is hindered by synthetic challenges. Specifically, oxides of the Sn(II) cation undergo facile oxidation to SnO₂ and/or disproportionation-driven decomposition to mixtures of Sn and SnO₂ at temperatures as low as 250 °C [13]. By comparison, PZT is

prepared by simple high temperature reactions of the binary oxides or in a molten flux at 700 °C and higher temperatures [14,15]. High temperature techniques are not compatible with Sn(II)-containing oxides or similar reactants, as Sn(II)-containing oxides are commonly metastable. One notable example is $SnTiO_3$, which was found in both experimental and theoretical studies to be metastable with respect to the ilmenite structure type [16–19]. Further, the ilmenite-type $SnTiO_3$ structure is metastable with respect to thermal decomposition to Sn_2TiO_4 and TiO_2 .

Despite these synthetic difficulties, low-temperature synthetic routes to new Sn(II)-containing oxides have been discovered in recent reported research efforts [8,17,20,21]. These recent approaches leverage low-temperature, kinetically-mediated pathways. A notable example, metastable Ba_{1-x}Sn_xZr_{1-v}Ti_vO₃ (BSZT) perovskite containing up to 60% Sn(II) cations, was prepared by reacting the Ba-containing perovskite (BZT) with a low melting SnClF peritectic flux [8]. The reaction is driven thermodynamically by the formation of BaClF from SnClF, enabling the formation of the metastable products at low reaction temperatures. The Zr(IV)-richer perovskite compositions were found to have a significantly higher synthetic Sn(II)-concentration limit than the Ti(IV)-richer perovskite compositions, although calculated to have similar metastability $(\sim 250-270 \text{ meV atom}^{-1} \text{ at } 60\% \text{ Sn(II)})$. Metastable phases are generally considered synthesizable if they lie within $\sim 100-200$ meV atom⁻¹ of the convex hull, but other factors impacting kinetic stability must also be considered [22,23]. For example, the higher lattice cohesive energy of cubic BaZrO₃ (-8.26 eV atom⁻¹) compared to cubic BaTiO₃ (-7.92 eV atom⁻¹) can act to increase the kinetic barrier to ion diffusion and thus hinder decomposition by phase segregation. Additionally, while the Zr(IV)-richer compositions decompose by phase segregation to ZrO2 and SnO, the decomposition of Ti(IV)-richer compositions to ilmenite-type SnTiO₃ requires significantly less ion diffusion. However, synthesizability factors such as these remain poorly explored for other possible Sn(II)-containing oxide perovskites.

Presented herein is an investigation of the synthesis of Sn(II)containing hafnate and stannate perovskites starting from pure $BaHfO_3$ and $BaSnO_3$. Low-temperature flux reactions were targeted to explore the Sn(II)-concentration limits in these perovskites, with the full replacement of Ba(II) for Sn(II) cations potentially yielding the metastable Sn^{II}Hf^{IV}O₃ and Sn^{II}Sn^{IV}O₃ perovskites. The BaHfO₃ perovskite has one of the largest calculated lattice cohesive energies $(-8.72 \text{ eV atom}^{-1})$ and which is hypothesized to yield a greater potential kinetic stabilization during these reactions. Conversely, the BaSnO3 perovskite has a significantly smaller lattice cohesive energy (-6.31 eV atom⁻¹). Prior theoretical reports on SnHfO3 show that it is metastable as a cubic or pseudocubic perovskite [24,25]. Additionally, the mixed-valent Sn₂O₃ perovskite, i.e., Sn^{II}Sn^{IV}O₃, has been calculated to be metastable with respect to layered structures and to decomposition-driven phase segregation to SnO and SnO₂ [26,27]. Currently, there are no prior reported syntheses of either of these perovskites. The products of the Sn(II)-exchange reactions, i.e., (Ba_{1-x}Sn_x)HfO₃ and (Ba_{1-x}Sn_x)SnO₃, are characterized by powder XRD, scanning transmission electron microscopy (S/TEM), and investigated for their synthesizability with increasing Sn(II), and including their thermal stability and decomposition pathways.

2. Experimental

2.1. Synthetic procedure

The barium hafnate precursor, $BaHfO_3$, was synthesized using high-temperature ceramic methods. First, hafnium (IV) oxide nanoparticles were synthesized by mechanical mixing of $HfCl_4$ (Acros Organics, 99%) with excess potassium hydroxide (VWR, 99.5%) under argon and washing with deionized water. The as-prepared HfO_2 nanoparticles were intimately mixed with a mortar and pestle with a 10% molar excess of $BaCO_3$ (Alfa Aesar, 99.8%), to account for volatilization, and pressed into a pellet. The reaction mixture was added to an alumina crucible and

reacted in a box furnace at 1500 °C for 48 h. The product was ground finely and reacted a second time as a pellet to obtain a pure, polycrystalline BaHfO₃ powder. The barium stannate perovskite, BaSnO₃, was synthesized via molten flux techniques. Similarly, a 10% molar excess of BaCO3 was finely ground with SnO2 (Alfa Aesar, 99.9%) and added to a eutectic mixture of NaCl (Fischer, > 99.5%) and KCl (Fischer, > 99.5%) in a covered alumina crucible. The mixture was reacted in a box furnace at 900 °C for 24 h. The obtained powder was washed with 150 mL of deionized water and dried at 80 °C overnight. The Sn(II)exchange reactions were performed by mixing the as-prepared BaHfO3 or BaSnO3 phases with a stoichiometric amount of a peritectic SnCl2/ SnF₂ mixture (Alfa Aesar; 99%, 97.5%, respectively) in a glovebox, until homogeneous. Next, the mixed powders were placed in an evacuated, fused-silica ampule and flame sealed. The reaction ampules were heated in a box furnace at various temperatures and times, from 250 °C to 350 °C and from 12 to 72 h. The products were washed with 150 mL of deionized water to remove the BaClF byproduct and any unreacted SnClF. The products were dried at 45 °C overnight. A typical reaction mixture did not exceed 100 mg in total mass. Additional reaction cycles followed the same protocol, with intermediate grinding under argon atmosphere before loading into a second reaction vessel.

2.2. Structural characterization techniques

Experimental XRD was measured on a Rigaku R-Axis Spider using a sealed X-ray Cu K α ($\lambda=1.54056$ Å, 40 kV, 36 mA) source in the Debye-Scherrer geometry with a curved image-plate detector. For the purposes of Rietveld refinement, additional XRD patterns were measured on a PANalytical Empyrean X-Ray diffractometer using Cu K α radiation ($\lambda_1=1.54056$ Å, $\lambda_2=1.544426$ Å, 45 kV, 40 mA) in the Bragg-Brentano geometry with a step size of 0.0131 in 2 θ and a 180 ms count time per step. High resolution synchrotron diffraction data sets were taken at the 11-BM-B beam line ($\lambda=0.457929$ Å) of the Advanced Photon Source (APS) at Argonne National Laboratory. Rietveld refinements of the data were performed using the General Structure Analysis System-II (GSAS-II) software to extract crystal structure information such as atomic occupancies and lattice parameters [28].

 $\it Ex\mbox{-}situ$ thermal decomposition experiments were carried out on a 40% Sn(II) sample, i.e., (Ba $_{0.6}$ Sn $_{0.4}$)HfO $_3$, prepared by reacting 80 mol% SnClF with BaHfO $_3$ under standard synthetic conditions listed previously. The sample was loaded into an evacuated, sealed, fused-silica ampule and annealed in a box furnace at temperatures at 200 °C for 1 h with a 10 °C min $^{-1}$ ramp rate and allowed to cool radiatively. The product was ground to homogenize before measurement of powder XRD at room temperature. The process is repeated in 50 °C steps as powder XRD data were collected from 200 °C to 500 °C.

2.3. Electron microscopy and energy dispersive spectroscopy

High resolution images and elemental analyses of BaHfO $_3$ were performed on a JEOL 6010LA scanning electron microscope (SEM) with an accelerating voltage of 20 kV. A JEOL EDXS silicon drift detector was used to determine elemental composition. High resolution images and elemental analyses of (Ba $_{1-x}$ Sn $_x$)HfO $_3$ materials were taken on an FEI Verios 460 L field emission scanning electron microscope (FESEM) and elemental analysis was measured with an attached Oxford energy dispersive X-ray spectrometer (EDS). Nanoscale resolution images were acquired using a ThermoFisher Talos F200X with 200 kV accelerating voltage. EDS spectra were collected using a 200 pA beam with a Super-X EDS detector and reported as net atomic intensities.

2.4. Electronic structure and total energy calculations

Density functional theory calculations of $(Ba_{1-x}Sn_x)MO_3$ (M = Sn or Hf) with x = 0.0, 0.25, 0.50, 0.75, and 1.0 were performed starting from $3 \times 3 \times 3$ supercells of the cubic perovskite structure using the *Vienna Ab*

initio Simulation Package (VASP; ver 4.6) using plane-wave density functional theory [29,30]. For compositions with Ba/Sn statistically mixed on the A-site, random positions within the supercell were chosen as Ba or Sn to achieve the desired stoichiometry. Total energy and densities-of-states calculations used the Perdew-Burke-Ernzerhof functionals in the generalized gradient approximation with the projector augmented wave method. A 3 \times 3 \times 3 Monkhorst-Pack grid was used to sample the Brillouin-zone automatically [31].

Calculations of the formation energies of the Sn(II)-containing perovskites followed the same protocol as reported previously by Hautier et al. and others [8,32,33]. These prior studies have demonstrated a relatively reliable accuracy in the calculation of formation energies (at 0 K) with a standard deviation of $\sim\!\!24$ meV atom $^{-1}$, which is much smaller than for the experimental errors of the measured reaction energies. Using this method, formation enthalpies of the metal-oxide perovskites were determined by total energy calculations using VASP at 0 K, in which the entropic term is negligible and thus $\Delta G_f \approx \Delta H_f$. Binary oxide formation enthalpies were obtained from the Open Quantum Materials Database (OQMD) [18,19]. An example calculation is shown below in Equations (1) and (2).

$$BaHfO_3(s) + SnClF(s) \rightarrow SnHfO_3(s) + BaClF(s)$$
 (1)

$$\Delta H_{rxn} = \left(\Delta H_{f(SnHfO_3)} + \Delta H_{f(BaCIF)}\right) - \left(\Delta H_{f(BaHfO_3)} + \Delta H_{f(SnCIF)}\right) \tag{2}$$

Decomposition energies for the solid solution perovskites, i.e., $Ba_{1.x}Sn_xHfO_3$, were similarly calculated. Decomposition reactions were balanced according to the experimental product distributions. For example, the Sn(II)-containing hafnate perovskite decomposes to SnO, HfO_2 , and $BaHfO_3$, as observed experimentally. An example reaction equation is shown below in Equation (3).

$$2(Ba_{0.5}Sn_{0.5})HfO_3 \rightarrow SnO + HfO_2 + BaHfO_3$$
 (3)

In this example, the complete decomposition and segregation of SnO results in the formation of the thermally stable BaHfO3. Further heating of SnO, however, results in its disproportionation into Sn metal and SnO2 under vacuum at temperatures $>\!300\,^{\circ}\text{C}$. In these cases, the presence of SnO2 was used as an indicator of SnO evolution when it was not observed at intermediate temperatures by XRD. All structural models and supercells used in this work were generated using the Visualization for Electronic and STructural Analysis (VESTA) software [34].

3. Results and discussion

3.1. Synthesis and bulk characterization

The barium hafnate perovskite was prepared by a high temperature ceramic route, resulting in a nominally pure and polycrystalline cubic phase with the stoichiometry BaHfO $_3$ (JCPDS 24–0102). Rietveld refinement in the $Pm\overline{3}m$ space group yielded a lattice parameter of

4.171428 (4) Å and wRp=7.99%, consistent with prior studies [35,36]. The barium stannate precursor was prepared using a NaCl/KCl eutectic synthesis route and yielded the polycrystalline BaSnO₃ cubic perovskite phase in high purity as well, with a refined lattice parameter of 4.11755 (3) Å and wRp=8.24%, consistent with prior reports (JCPDS 150780) [37]. Both BaHfO₃ and BaSnO₃ perovskites were reacted separately in the SnClF flux, aiming at the Sn(II)-richest perovskites having the respective compositions (Ba_{1-x}Sn_x)HfO₃ and (Ba_{1-x}Sn_x)SnO₃ (*vide infra*), as represented in Fig. 1 and in Reaction 4 below:

$$BaMO_3 + x SnClF \rightarrow (Ba_{1-x}Sn_x)MO_3 + x BaClF \quad (M = Hf \text{ or } Sn)$$
 (4)

The calculated energy change of the reactions are −270.8 kJ mol⁻¹ (-2.81 eV/F.U.) for BaHfO₃ \rightarrow SnHfO₃ and -285.6 kJ mol⁻¹ (-2.96 eV/F.U.) for $BaSnO_3 \rightarrow SnSnO_3$, demonstrating that both reactions are thermodynamically favorable. The Sn(II)-halide flux melts beginning at ~200 °C facilitating its reactivity at low temperatures, coupled with the thermodynamic driving force of the formation of BaClF versus SnClF (-1028 kJ mol⁻¹), as reported previously [8]. Both the SnClF reactant and BaClF side product are water soluble and can be removed from the product by washing. A comparison of selected XRD patterns of Sn(II)-substituted perovskites is shown in Fig. 2, with the (Ba_{1-x}Sn_x)HfO₃ series shown on the left and (Ba_{1-x}Sn_x)SnO₃ series shown on the right, where x is the mole fraction of reacted SnClF at 250 °C for 72 h. As shown in Fig. 2, the $Pm\overline{3}m$ perovskite reflections remain nearly constant in each as the mole fraction of Sn(II) increases. Impurity peaks of tin oxides start to be detected as low as 10% reacted SnClF with (Ba_{1-x}Sn_x)SnO₃, corresponding to immediate phase decomposition. In contrast, decomposition was not observed in (Ba_{1-x}Sn_x)HfO₃ up to 100% SnClF concentration, but only at an excess of 130% reacted SnClF. These XRD results are consistent with a much higher kinetic stability for the Sn(II)-containing hafnate perovskite.

3.2. Electron microscopy

Electron microscopy techniques were employed to assess the Sn(II)-content and compositional homogeneity of the $(Ba_{1-x}Sn_x)HfO_3$ perovskites. SEM and FESEM images of the particles' sizes and morphologies for x=0, 0.7 and 1.0 are provided in Fig. S3. These data reveal that the solid-state synthesis of BaHfO₃ produces crystallites with dimensions ranging from ~ 1 to 5 μ m and relatively smooth surfaces. After reaction with SnClF, i.e., for x=0.7 and 1.0, the particles become much smaller and more nanocrystalline. Some larger particles have formed by agglomeration, but these also occur together with substantially more nanoscale particles.

Energy-dispersive spectroscopy (EDS) on the particles showed a significant dependence on the Sn/Ba homogeneity with the chosen reaction temperature and time. The EDS data for the first set of reaction conditions, i.e., 250 °C for 72 h, are shown for x=0.7 (nominally 70 mol% Sn(II)) in Fig. 3. The chemical maps reveal a relatively inhomogeneous Ba

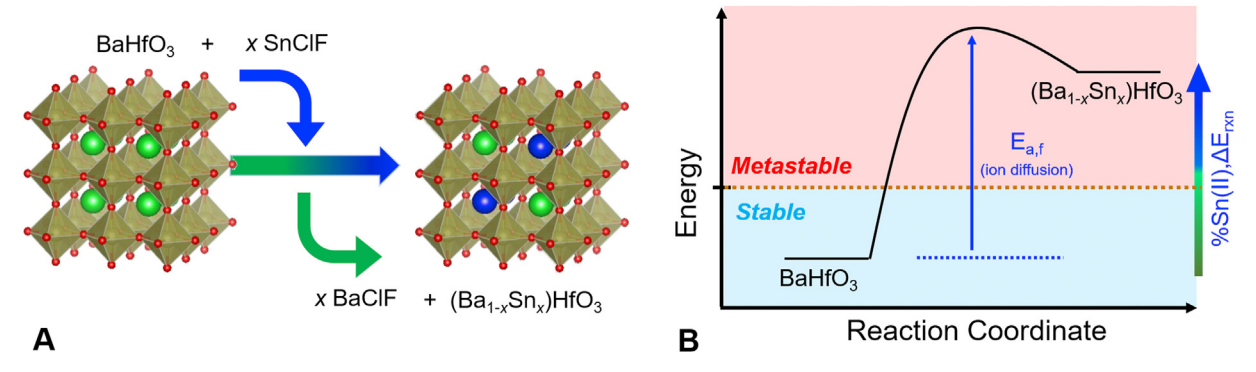


Fig. 1. Schematic representation of low temperature flux exchange reaction of BaHfO₃ (left) and relative energy of $(Ba_{1.x}Sn_x)HfO_3$ products. The barium perovskite reacts with SnClF to replace Ba(II) and give the $(Ba_{1.x}Sn_x)HfO_3$ product. As more Sn(II)-cations exchange, the perovskite becomes increasingly metastable.

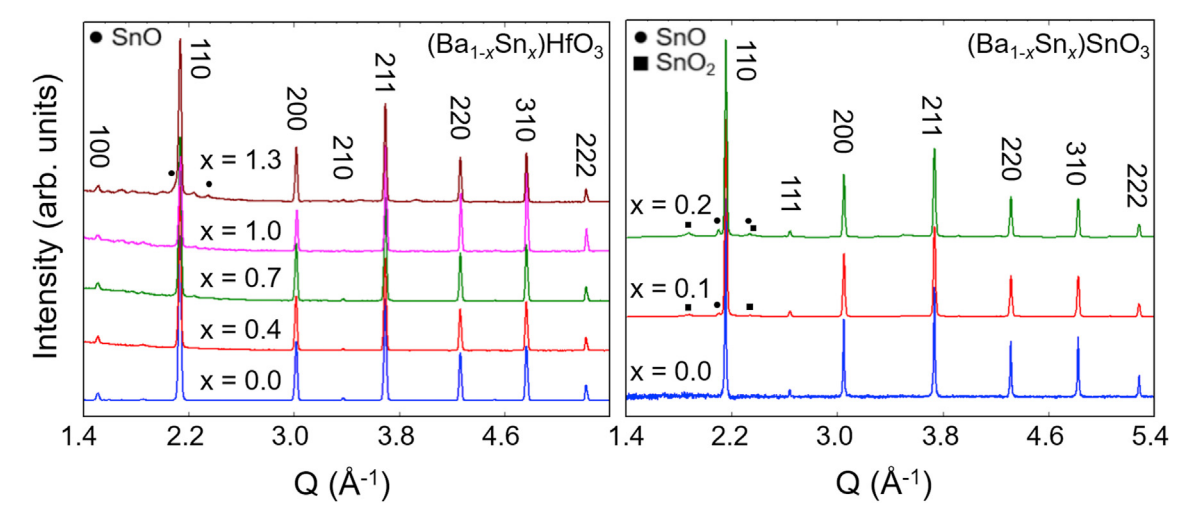


Fig. 2. XRD patterns of the $(Ba_{1.x}Sn_x)HfO_3$ (left) and $(Ba_{1.x}Sn_x)SnO_3$ (right) perovskite powders, where x indicates the nominal mole fraction of Sn(II). Secondary phases of SnO an SnO₂ are labeled with black circles and squares, respectively.

and Sn distribution, with the separation of Ba-rich and Sn-rich regions being observed as a result of inhomogeneous diffusion of Sn(II). Inhomogeneity is apparent when comparing the compositions of primary particles within the larger aggregates. The Sn(II) diffusion typically terminates to within $\sim \! 100$ nm of the surfaces of the larger particles. A homogenous distribution of the Ba, Hf, Sn, and O elements were obtained only with the smallest observed particles, i.e., $< \! 100$ nm in diameter, with no detectable regions of elemental segregation, shown in Fig. S4. By contrast, the distribution of Hf and O (not shown) is relatively homogeneous across all particle sizes and shapes, supporting the persistence of the underlying hafnate perovskite structure and the absence of phase segregation. The EDS results are consistent with the Sn(II)-concentration being limited by its ion diffusion through the perovskite structure at 250

°C.

To test the impact of temperature on the Sn(II) diffusion, the flux-based reactions were repeated at a higher temperature but shorter time of 350 °C for 12 h, similar to the conditions reported for the analogous BSZT perovskites. EDS maps of $(Ba_{1-x}Sn_x)HfO_3$ products for x=0.7 are shown in Fig. 4. At the higher temperature, the Sn(II)-exchange reactions result in a significantly more homogeneous Ba/Sn distribution for even the largest particle sizes. While the higher temperature increases the Sn(II) diffusion, the increased thermal energy also causes significantly more decomposition. Shown in Fig. 4e (inset), the product formed at the higher reaction temperature of 350 °C has turned a dark black color, whereas the sample prepared at the lower 250 °C is yellowish. At this nominal 70 mol% Sn(II) concentration, the lower temperature reaction

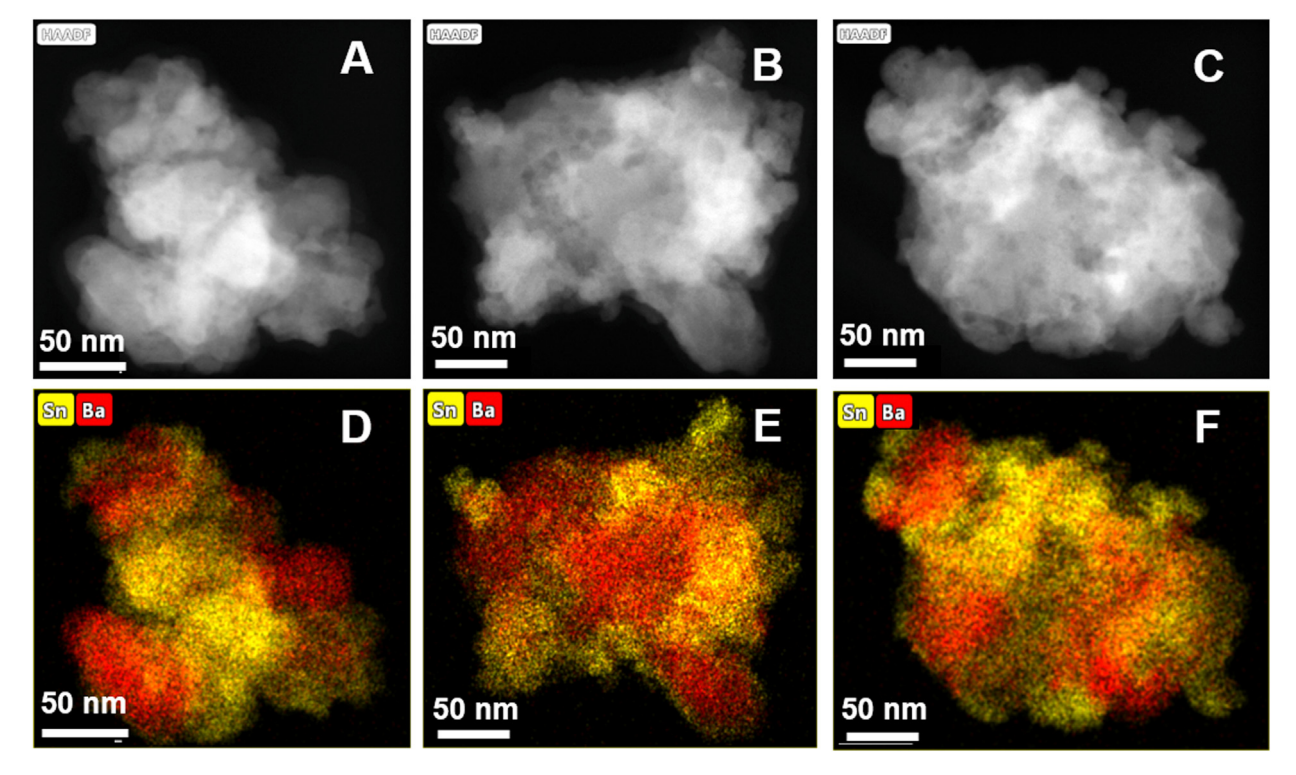


Fig. 3. High-angular dark field images (A–C) and elemental mapping (D–F) of the Ba and Sn contributions, red and yellow colored respectively, within three different particles after a reaction with a nominal 70% Sn(II) reacted at 250 °C for 72 h. (For interpretation of the references to color in this figure legend, the reader is referred to the Web version of this article.)

produces no detectable impurities while the high temperature synthesis yields $\sim\!\!10\%$ of dark black SnO impurity, (Fig. 4e insets). The higher temperature reaction provides a more homogeneous Sn(II) distribution in a shorter time, although coming at the expense of increased decomposition.

A third set of reaction conditions was tested which involved a second cycle of mechanical homogenization and heating the reaction mixture at 250 °C for 72 h. The additional reaction cycle was implemented to facilitate the Sn(II) diffusion but at the possible expense of further product decomposition. EDS data are shown in Fig. 5a for the nominally x=0.7 composition, i.e., $\mathrm{Ba_{0.3}Sn_{0.7}HfO_3}$, for a relatively large particle agglomerate with ~10–20 µm diameter. Analogous EDS data for the nominally x=1.0 product, i.e., $\mathrm{SnHfO_3}$, are provided in Fig. 5b. A homogeneous distribution of $\mathrm{Sn(II)}$ is observed throughout both particles as shown in the elemental mapping. Fig. 5 shows representative particles with a high sample purity and homogeneous $\mathrm{Sn(II)}$ distribution that can be achieved at the lower temperature with one additional grinding and heating step.

The chemical compositions obtained from EDS analysis are listed in Table 1 for the lower temperature products at 250 °C for 72 h after heating one or two cycles. In each case, the EDS spectrum of BaHfO₃ was used as an internal standard. The data in Table 1 show a trend with increasing amounts of Sn(II) in the perovskite with increased nominal amounts in the reaction and with the number of heating cycles. After a single reaction cycle with 70 mol% Sn(II) at 250 °C, the amount of Sn(II) exchanged, as evidenced by EDS, is about half of that, ranging from ~30 to 50%, or ~38% on average. At the ~(Ba2/3Sn1/3)HfO3 composition there are no detectable impurity phases in the XRD patterns, consistent with a perovskite phase with Ba(II) and Sn(II) cations co-occupying the A-site at about the $(Ba_{2/3}Sn_{1/3})HfO_3$ stoichiometry. After two reaction cycles are performed with a nominal 70 mol% Sn(II), with secondary grinding, the amount of Sn in the product increases to ~49% with no change in the XRD pattern. When the BaHfO₃ precursor is reacted twice with a nominal 100 mol% Sn, the amount of Sn(II)-cations exchanged by EDS increases to a relatively larger amount of \sim 70%. The (Ba_{0.3}Sn_{0.7}) HfO₃ phase is the highest amount of Sn(II) attained in the perovskite structure without detection of significant impurity phases in the XRD patterns. For the higher temperature reactions at 350 $^{\circ}\text{C},$ the mole fractions of Ba/Sn could not be reliably determined because of the formation

of high amounts of impurity phases. Thus, the collective XRD and EDS results suggest that the synthetic limit of Sn(II) exchange into the perovskite for these reaction conditions is a conservative $\sim 70\%$, or $(Ba_{0.3}Sn_{0.7})HfO_3$, with growing amounts of decomposition occurring upon further exchange, and is the closest attainable to the highly metastable $SnHfO_3$ perovskite that can be synthesized under these conditions.

3.3. Structural characterization

Rietveld refinements were performed on powder XRD patterns measured on the PANalytical Empyrean diffractometer for the Sn(II)containing hafnate perovskite compositions with mole fractions of Sn(II) at x = 1/3, 1/2, and 2/3 as determined by EDS analyses. The resulting fits to the data for the $(Ba_{2/3}Sn_{1/3})HfO_3$ and $(Ba_{1/3}Sn_{2/3})HfO_3$ phases are displayed in Fig. 6. The figure shows that the main Bragg peaks of the cubic perovskite structure are maintained with Sn(II) substitution. Rietveld refinements were performed in the $Pm\overline{3}m$ space group and a summary of selected refined parameters is provided in Table 2. There is a small decrease in lattice constant with increasing Sn(II)substitution and the refinements are in good agreement with cubic symmetry. The refined atomic A-site occupancy fractions for Sn(II) increase with increasing nominal Sn(II) substitution and are comparable to the values determined by EDS. To obtain as stable a refinement as possible, the Ba/Sn fractional occupancies were constrained to sum to one and were refined independent from the atomic displacement parameter (U_{iso} value). In addition to the primary perovskite phase, some background peaks were observed in the pattern, but were less than $\sim 1\%$ relative intensity and thus difficult to use for phase identification.

Synchrotron powder XRD patterns were measured on the $(Ba_{2/3}Sn_{1/3})$ HfO $_3$ phase to further investigate the main phase and background peaks with higher resolution, shown in Fig. S9. Between 5 and $15^{\rm o}$ 20, several small peaks are observed with less than 0.5% relative intensity. Most of these peaks were identified as trace amounts of impurities of SnO, BaClF, and BaCl $_2(H_2O)_2$ and their refined phase fractions summed to approximately 4% of the total pattern. A Rietveld refinement was performed with a primary cubic perovskite phase combined with the identified impurity phases, resulting in a weighted residual of 8.73% and a reduced χ^2 of 2.79. The primary peaks agree with the cubic $\mbox{\it Pm}\mbox{\it 3m}$ space group with a lattice parameter of 4.173399 (3) Å. A high-resolution pattern of

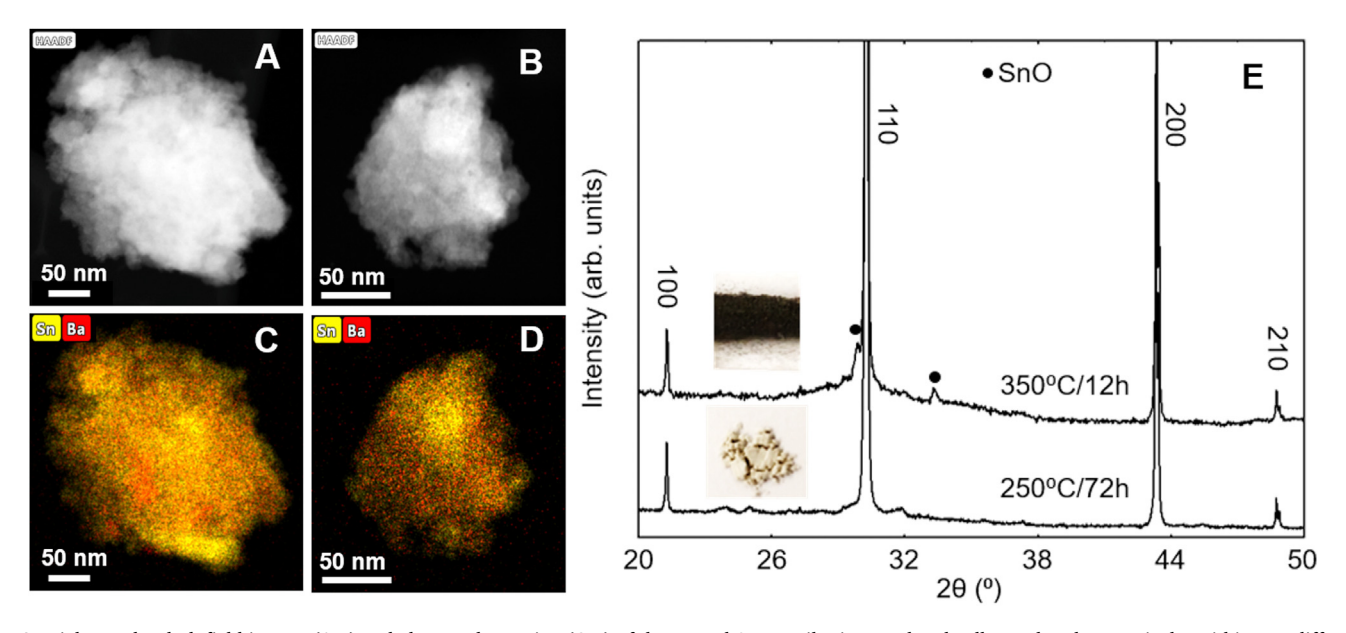


Fig. 4. High-angular dark field images (A,B) and elemental mapping (C,D) of the Ba and Sn contributions, red and yellow colored respectively, within two different reactions with a nominal 70% Sn(II) reacted once at 350 °C for 12 h. Shown in (E) is the comparative powder XRD of products from reactions run at 250 °C for 72 h and 350 °C for 12 h, with 70% Sn(II), with the powder colors shown in the insets. (For interpretation of the references to color in this figure legend, the reader is referred to the Web version of this article.)

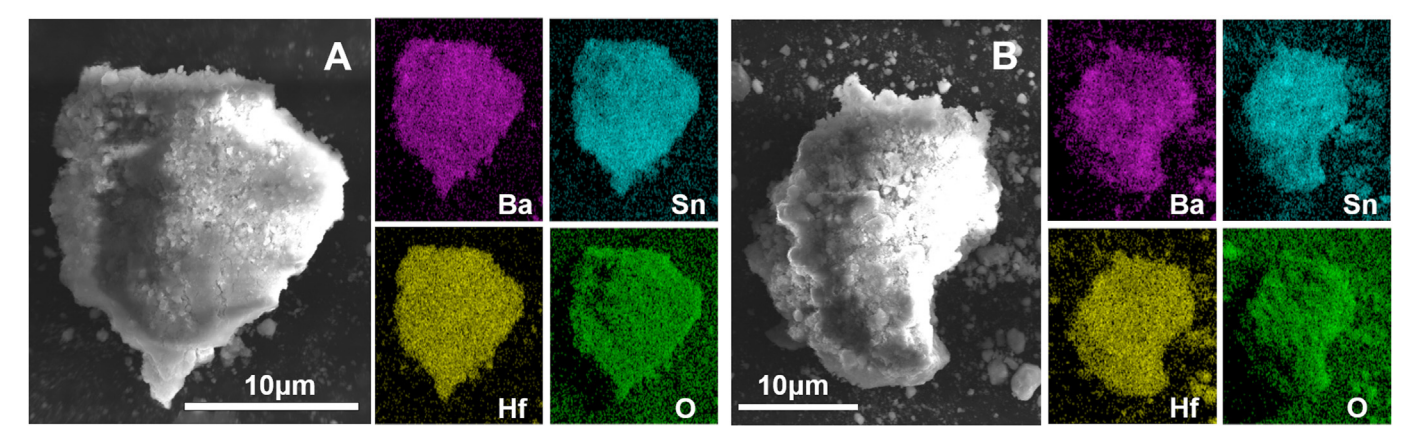


Fig. 5. FESEM/EDS images of representative particles of reactions with a nominal 70% Sn(II) (left) and 100% Sn(II) (right) after two repeated flux reactions at 250 °C for 72 h each. Elemental maps are shown on the right, with Ba denoted as purple, Sn as light blue, Hf as yellow, and O as green. (For interpretation of the references to color in this figure legend, the reader is referred to the Web version of this article.)

Table 1 Tabulated results of EDS data for $(Ba_{1-x}Sn_x)HfO_3$ as a function of the nominal Sn(II) amount, (x), after heating to 250 °C for 72 h for either one or two heating cycles.

Element	$x_{nom} = 0.7 (1 \text{ cycle})$	$x_{nom} = 0.7$ (2 cycles)	$x_{nom} = 1.0 (2 \text{ cycles})$
Ba mol %	33.40	25.97	16.49
Sn mol %	20.12	24.98	39.04
Sn:Ba ratio	0.602	0.962	2.368
x_{\exp} (Ba _{1-x} Sn _x)	0.38	0.49	0.70
HfO_3	$Ba_{0.62}Sn_{0.38}O_3$	$Ba_{0.51}Sn_{0.49}O_3$	$Ba_{0.3}Sn_{0.7}O_3$

the precursor, BaHfO₃, was also measured and refined to a lattice parameter of 4.173434 (2) Å. While the precursor BaHfO₃ has a slightly larger lattice constant after $\sim\!1/3$ Sn(II)-substitution, this difference is likely not statistically significant owing to errors inherent in the instrumental parameters.

3.4. Metastability and thermal decomposition pathway

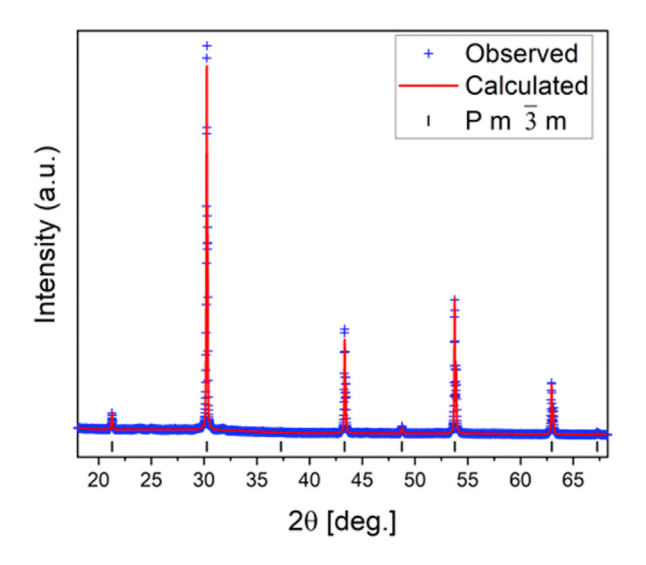
The extent of kinetic stabilization of the $(Ba_{1.x}Sn_x)HfO_3$ perovskites was investigated using both *ex situ* and *in situ* characterization methods during heating. As metastable phases, evidence of being kinetically

Table 2 Summary of refined parameters from laboratory powder XRD measurements for Sn(II)-hafnate perovskites in the $Pm\overline{3}m$ space group.

Composition	$Ba_{2/3}Sn_{1/3}HfO_3$	$Ba_{1/2}Sn_{1/2}HfO_3$	$Ba_{1/3}Sn_{2/3}HfO_3$
Ba Fraction	0.71 (2)	0.63 (3)	0.40 (4)
Sn Fraction	0.29(2)	0.37(3)	0.60 (4)
a (Å)	4.17213 (3)	4.17206 (6)	4.17168 (6)
$V(Å^3)$	72.623 (2)	72.619 (3)	72.600 (3)
wRp (%)	4.80	3.55	3.80
Rp (%)	3.55	2.65	2.83
Reduced χ^2	6.27	3.75	4.10

trapped at a higher energy than the ground state can be experimentally probed under elevated temperatures that provide sufficient thermal diffusion for the ions to diffuse and reach the ground state, i.e., to decompose to the simpler oxides. Thus, for the current perovskite products discussed above, the decomposition reaction most typically occurs as $\text{AMO}_3 \rightarrow \text{AO} + \text{MO}_2$. The degree of metastability and the decomposition pathway has been assessed at increasing temperatures by heating in a furnace with ex-situ XRD as well as by heating under an electron beam using in situ S/TEM methods. Decomposition of the stannate perovskites were observed during the Sn(II)-exchange reactions and described earlier.

Shown in Fig. 7 is ex situ powder XRD data in which the (Ba_{0.6}Sn_{0.4})



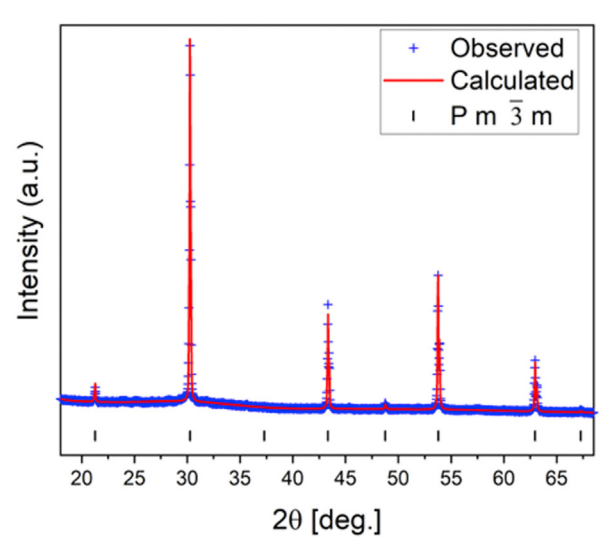


Fig. 6. Rietveld refinements of $(Ba_{2/3}Sn_{1/3})HfO_3$ powder XRD data (left) and $(Ba_{1/3}Sn_{2/3})HfO_3$ (right) according to the cubic perovskite structure in the $Pm\overline{3}m$ space group.

HfO₃ perovskite with 40% Sn(II) cations was heated from 50 °C to 500 °C under vacuum in 50 °C increments with intermediate grinding and XRD measurements. Powder XRD data were linearly interpolated between each set. As shown by the primary reflection at ~26°, SnO2 (cassiterite type) starts forming in growing amounts by 350 °C. This diffraction peak increases in intensity with increasing temperature, along with two of its next most intense peaks at ~32-34° appearing by ~375 °C. Under vacuum, the formation of SnO₂ is from the concurrent disproportionation of SnO which begins rapidly by ~300 °C, in agreement with previous reports [38,39]. The sample also begins to change significantly in color, starting as a light-yellow powder at room temperature and turning entirely black colored by 400 °C. The color change is the result of the amorphous Sn metal that also forms during the disproportionation reaction of SnO. By \sim 400 °C, the XRD patterns also show that HfO₂ crystallizes out beginning at ~400 °C, as evidenced by the intense diffraction peaks at ~28.1° and ~31.6°. Impurity peaks corresponding to residual SnClF and BaClF also appear in the data, likely because of being adsorbed to particle surfaces, and which repeated aqueous washing did not effectively remove. Fig. 7 shows that, in the 400-425 °C range, the Sn(II)-exchanged barium hafnate begins decomposing into HfO2 and SnO, with the perovskite reflections still present. As the BaHfO₃ perovskite is thermodynamically stable and high melting (m.p. \sim 2620 $^{\circ}$ C), the decomposition pathway is driven by the removal of Sn(II) cations from the structure.

Decomposition of the most Sn(II)-rich phase, (Ba_{1/3}Sn_{2/3})HfO₃, was probed using S/TEM methods to observe fine-level changes at the surfaces of individual nano-crystallites that cannot be detected in XRD. Shown in Fig. 8 are the S/TEM and EDS images of a representative particle after partial electron-beam induced decomposition at its surfaces. After its partial decomposition, four separate regions are apparent as a result of phase segregation, labeled A to D. In region A, the EDS data yield an approximate composition of (Ba_{1/2}Sn_{1/2})HfO₃, which is slightly Sn(II)-deficient as compared to the starting composition. Extending outward, the elemental mapping (colored) in regions B and C show evidence for phase segregation, respectively, into BaHfO₃ and then a mixture of SnO and HfO₂. Only Sn and O are observed in the outermost region D, corresponding to either a mixed-valent tin oxide phase or to a mixture of SnO₂ and elemental Sn. The latter interpretation is consistent with the powder XRD results described above, as owing to the

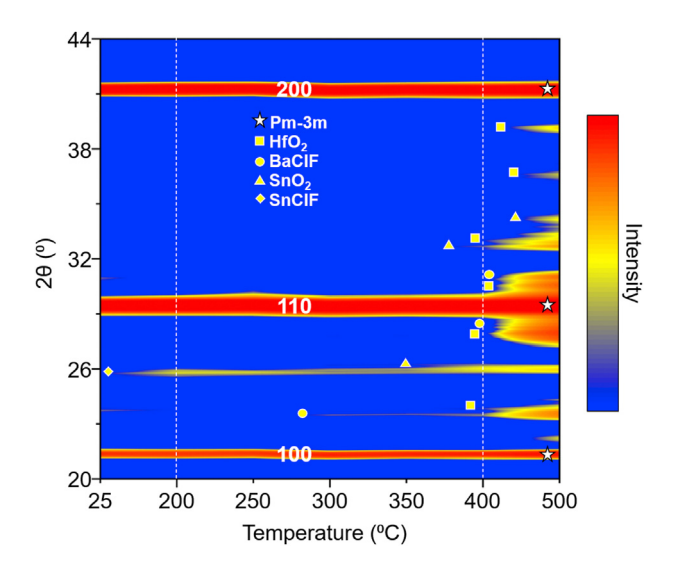


Fig. 7. Ex situ XRD of $Ba_{0.6}Sn_{0.4}HfO_3$ at temperatures between 25–500 °C. Diffraction data shown for the 20– 44° 20 range. Perovskite reflections from $(Ba_{0.6}Sn_{0.4})HfO_3/BaHfO_3$ are labeled by stars with hkl indices, HfO_2 by squares, BaClF by circles, SnO_2 by triangles, and SnClF by diamonds. BaClF and SnClF are left over from the formation reaction and were not sufficiently removed via washing.

disproportionation of SnO. The *ex situ* and *in situ* experiments have demonstrated, both in the average structure measured from diffraction and down to a fine-level surface detail in microscopy, a decomposition pathway of the metastable perovskite that is driven by phase segregation and is consistent with the following reactions:

$$Ba_{1-x}Sn_xHfO_3 \rightarrow x SnO + xHfO_2 + (1-x)BaHfO_3$$
 (5)

$$x\text{SnO} \rightarrow x/2 \text{SnO}_2 + x/2 \text{Sn}$$
 (6)

The decomposition results are also consistent with the synthetic reaction conditions. A low reaction temperature of $\sim\!250~^\circ\text{C}$ is critical to trap the metastable hafnate perovskites, as slightly higher temperatures of $\sim\!350~^\circ\text{C}$ are found to result in significant decomposition. The kinetic stabilization of the metastable perovskites is thus dependent upon minimizing ion diffusion within the crystallites, and specifically, the diffusion of Sn(II) cations. In contrast, the analogous stannate perovskites, i.e., (Ba_{1-x}Sn_x)SnO₃, decomposed under the same synthetic conditions. The immediate decomposition is a consequence of the underlying perovskite framework being based on Sn(IV) cations, and when Ba(II) is exchanged with the Sn(II) cations, there is much less ion diffusion required for phase segregation to SnO₂ and SnO (e.g. O–Sn^{II}–O local ordering).

3.5. Calculations of metastability

Using methods established previously by Hautier and others, total energy calculations were performed using density functional theory in _rSn_r)HfO₃ perovskites with increasing Sn(II) content [8,32,33]. Results of the calculations show that as Sn(II) is increasingly incorporated into the A-site the total energy decreases nearly linearly ($R^2 = 0.995$) with the Sn(II) concentration, from -8.722 eV atom⁻¹ in BaHfO₃ (0% Sn(II)) to -8.205 eV atom⁻¹ in SnHfO₃ (100% Sn(II)). The calculated total energy for BaHfO3 agrees with prior published data (online) in the Open Quantum Materials Database of -8.715 eV atom⁻¹ [18,19]. While BaHfO₃ is shown to be thermodynamically stable against decomposition, the thermal decomposition corresponding to Reaction 5 (given above) becomes increasingly favorable with increasing Sn(II) amounts for $(Ba_{1-x}Sn_x)HfO_3$ beyond ~10 mol% Sn. For example, for only ~25% Sn (x = 0.25), the perovskite composition is already highly metastable by about -156 meV atom⁻¹ towards decomposition by phase segregation, e.g., 4 (Ba_{3/4}Sn_{1/4})HfO₃ \rightarrow 3 BaHfO₃ + SnO + HfO₂. For even higher Sn(II) amounts, the decomposition energies increase to -312 meV atom⁻¹, -479 meV atom⁻¹ and -647 meV atom⁻¹, for x = 0.5, 0.75, and 1.0, respectively. The trend in decomposition energies is consistent with the experimentally observed decomposition reactions. It is generally reported that metastable compounds can potentially be synthesized that fall within $\sim 100-200 \text{ meV atom}^{-1}$ of the ground state [22,23]. The current results show that this range is greatly exceeded for the highest synthesized Sn(II)-containing perovskite, Ba_{0.3}Sn_{0.7}HfO₃ with a calculated metastability of about -446 meV atom⁻¹. The extremely high melting point of the reactant perovskite, BaHfO3 (m.p. ~2620 °C), suggests that ion diffusion and therefore phase segregation is highly inhibited at low temperatures, as discussed below.

The stannate perovskites are similarly found to become increasingly thermodynamically unstable towards decomposition by phase segregation. The B-site cation is fixed as Sn(IV) and the flux reaction causes substitution of the Sn(II) cations onto the A-site. The total energy of (Ba₁. $_x$ Sn $_x$)SnO₃ increases linearly with the Sn(II) amount on the A-site from -6.306 eV atom⁻¹ for 0% Sn(II) in BaSnO₃ to -5.819 eV atom⁻¹ for 100% Sn(II) in Sn^{II}Sn^{IV}O₃ in the cubic perovskite structure. The decomposition pathways were modeled analogous to the hafnate perovskites, i.e., as (Ba_{1-x}Sn $_x$)SnO₃ \rightarrow (1-x) BaSnO₃ + x SnO + x SnO₂. The results show that the Sn(II)-substituted perovskites again become substantially more metastable as the amount of Sn(II) increases with respect

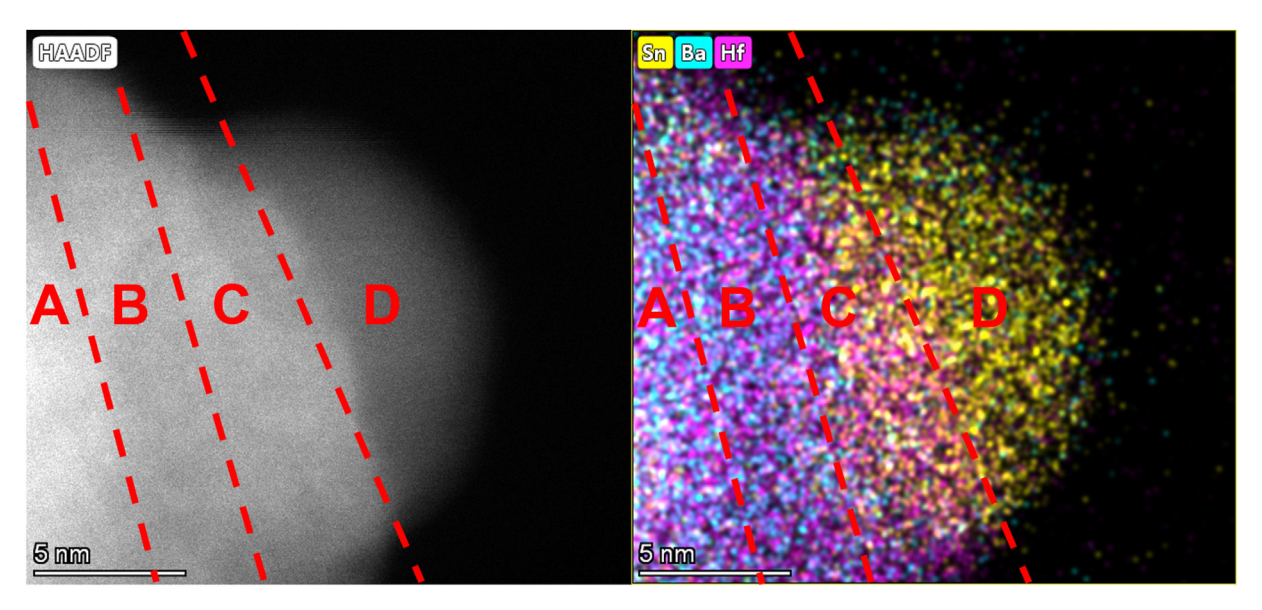


Fig. 8. S/TEM image of perovskite nano-crystallite after electron-beam induced phase segregation. EDS data show that the composition within the (marked) region A is the (Ba,Sn)HfO₃ perovskite, region B is BaHfO₃, region C is HfO₂ and SnO, and region D is Sn and SnO₂.

to decomposition by phase segregation. The decomposition energy for BaSnO₃ is calculated to be $+183~{\rm meV}$ atom⁻¹, showing that it is thermodynamically stable. For increasing amounts of Sn(II) of $x=0.25, 0.5, 0.75, {\rm and}\ 1.0$, the decompositions energies were found to be $-122~{\rm meV}$ atom⁻¹, $-244~{\rm meV}$ atom⁻¹, $-381~{\rm meV}$ atom⁻¹, and $-519~{\rm meV}$ atom⁻¹. Thus, the barium stannate perovskites are all less metastable than the corresponding hafnate perovskites, despite not being as nearly synthesizable. Reactions intended at each of these compositions decompose nearly entirely to the phase-segregated products, clearly suggesting significant differences in the kinetic barriers of their decomposition pathways.

Shown in Fig. 9 are schematic diagrams of the energetics of the decomposition pathways of the (Ba_{1-x}Sn_x)HfO₃ and (Ba_{1-x}Sn_x)SnO₃ as a function of the amount of Sn(II), as well as the empirically estimated relative activation barriers based upon the observed decomposition of BaHfO₃ and BaSnO₃ at the synthetic limits of the Sn(II) concentrations in each. The (Ba_{1-x}Sn_x)HfO₃ is shown to have a significantly higher activation barrier against decomposition as compared to (Ba_{1-x}Sn_x)SnO₃, as reflecting the greater kinetic stabilization and synthesizability. One factor leading to the seemingly absent activation barrier of the (Ba_{1-x}Sn_x) SnO₃ perovskite is the greater overall concentration of Sn, i.e., containing both Sn(IV) and Sn(II) cations, and that reduces the diffusion lengths needed for phase segregation to occur. However, another prominent factor is the significantly higher cohesive energy of the reactant BaHfO3 versus BaSnO₃ perovskite. A recent study of the analogous BSZT perovskite system showed a higher Sn(II)-exchange limit for the Zr-richer compositions, which was hypothesized to be the result of a trend toward a greater lattice cohesive energy. The calculated difference in lattice energies were quite small, i.e., -39.6 eV atom⁻¹ and -40.9 eV atom⁻¹ for BaTiO3 and BaZrO3, respectively. By comparison, BaHfO3 and BaSnO3 have much larger and smaller cohesive energies, respectively. These energies are listed in Table 3 along with the observed limit of Sn(II) concentration for each perovskite system.

Prior theoretical studies have found the cohesive energy is an important variable to calculate the average amplitude of thermal vibrations within the Lindemann criterion [40,41], which posits that melting occurs, and hence significant ion diffusion, when the lattice vibrations exceed a threshold value that generally increases with the lattice cohesive energy. As listed in Table 3, as the lattice cohesive energies increase from the low extreme of BaSnO₃ to the high extreme of BaHfO₃ of -43.6 eV atom⁻¹. These generally correspond to relatively lower and higher melting points with some deviations from the expected trend. However,

the Sn(II)-exchange limit increases proportionally from <10% to ~70%, more closely following the trend with increasing lattice cohesive energy than do the melting points. The two perovskites with the smallest cohesive energies exhibit very low synthesizability of their metastable Sn(II)-containing analogues under these conditions. Notably, both can also decompose by routes that involve minimal ion diffusion, such as with the occurrence of ilmenite-type SnTiO₃ that competes for formation in the (Ba_{1-x}Sn_x)TiO₃ perovskite system. Thus, favorable conditions to prepare the most metastable Sn(II)-containing perovskites include both high lattice cohesive energies as well as the existence of lower-energy competing phases that require maximal ion diffusion to reach.

4. Conclusions

Low temperature flux-mediated reactions of SnClF show that the exchange of Sn(II) for Ba(II) cations in BaHfO3 and BaSnO3 can yield significant Sn(II)-cation incorporation only in the former, yielding (Ba₁. $_x$ Sn $_x$)HfO $_3$ at up to $x \sim 0.7$. Electron microscopy imaging shows that the highest concentration of Sn(II) cations of ~70% with a homogeneous distribution can only be achieved at low reaction temperatures of ~250 °C with two consecutive reactions and intermittent grinding. Analogous cation-exchange reactions for the stannate perovskite only resulted in its decomposition. The metastable (Ba_{1-x}Sn_x)HfO₃ compositions exhibit a decomposition pathway that proceeds at its surfaces via phase segregation into the simpler oxides, beginning at only ~350 °C. Total energy calculations demonstrate the highest metastability of the ~70% Sn(II) perovskite, $(Ba_0 \, _3Sn_0 \, _7)HfO_3$, reaches a remarkable ~ -446 meV atom⁻¹ against decomposition, which is significantly higher than previously considered for being synthesizable. The additional kinetic stabilization of the hafnate perovskites is posited to result from its much higher high cohesive energy, melting point, and the absence of lower-energy polymorphs or a ground state that could potentially be reached without requiring significant ion diffusion. The presented results have helped to elucidate the relationship between the synthesizability and metastability of Sn(II)-containing perovskites that have been long desired as a new class of technologically relevant materials. Discovery of the key factors leading to the successful synthesis of Sn(II)-containing metastable perovskites will hopefully lead to the synthesis of the first high-purity Sn(II)-only SnMO₃ perovskites in the future. For example, reactions to target a more complete Sn(II)-cation exchange are currently under investigation using synthetic approaches which can increase both the extent and rates of cation diffusion at lower temperatures. These

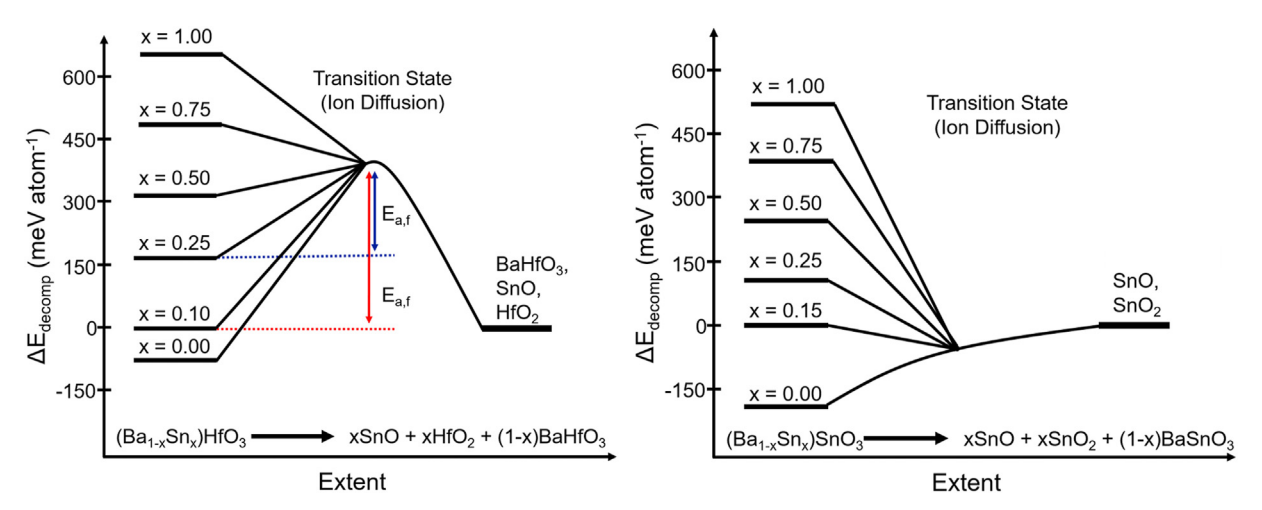


Fig. 9. A schematic of the calculated energy above ground state (i.e., metastability) for (left) $(Ba_{1.x}Sn_x)HfO_3$ and (right) $(Ba_{1.x}Sn_x)SnO_3$. The energy of decomposition increases with %Sn(II), becoming metastable at $x \approx 0.15$ in the stannates and $x \approx 0.1$ in the hafnates. The relative $E_{a,f}$ was estimated based upon the concentration of Sn(II) that exchanges before the onset of decomposition.

Table 3
Listing of perovskite cohesive energies and melting points compared to the synthesizable Sn(II)-containing perovskites and the extent of their metastability compared to the ground state.

Perovskite Composition	Cohesive Energy (eV atom ⁻¹)	Melting Point (K)	Maximum Sn(II) Concentration(mol %)	ΔE_{Decomp} at Max $Sn(II)$ (meV $atom^{-1}$)
BaSnO ₃	-31.5	2128	<10	≤0
$BaTiO_3$	-39.6	1898	10	≤0
$BaZrO_3$	-40.9	2923	50	+225
BaHfO ₃	-43.6	2893	70	+446

strategies include increasing the concentration of A-site and/or B-site cation vacancies as well as decreasing the particle sizes.

Supporting information

Additional experimental data are provided including powder XRD data of the BaHfO3 and BaSnO3 perovskite precursors, before and after reaction Sn(II)-substituted BaHfO3, the (Ba1,xSnx)HfO3 products after two reaction cycles, and results of the multi-phase Rietveld refinement of synchrotron XRD results. Additional S/TEM images of (Ba1,xSnx)HfO3 are provided, including Hf and O elemental mapping, EDS of electron-beam induced phase segregation, and selected area electron diffraction (SAED) images of the perovskite and secondary phase.

CRediT authorship contribution statement

Eric A. Gabilondo: Investigation, sample synthesis, computation, DFT, Writing – review & editing. Shaun O'Donnell: Conceptualization, reviewing. Rachel Broughton: Structure determination, Conceptualization, reviewing. Jacob L. Jones: Conceptualization, Methodology, reviewing. Paul A. Maggard: Conceptualization, Methodology, writing, reviewing.

Declaration of competing interest

The authors declare that they have no known competing financial interests or personal relationships that could have appeared to influence the work reported in this paper.

Acknowledgements

The authors acknowledge support of this work by the National Science Foundation (DMR-2004455). A portion of this research used resources of the Advanced Photon Source, a U.S. Department of Energy (DOE) Office of Science User Facility operated for the DOE Office of Science by Argonne National Laboratory under Contract DE-AC02-06CH11357. Extraordinary facility operations were supported in part by the DOE Office of Science through the National Virtual Biotechnology Laboratory, a consortium of DOE national laboratories focused on the response to COVID-19, with funding provided by the Coronavirus CARES Act. Additional components of this research were performed in part at the Analytical Instrumentation Facility (AIF) at North Carolina State University, which is supported by the State of North Carolina and the National Science Foundation (Award ECCS-2025064). The AIF is a member of the North Carolina Research Triangle Nanotechnology Network (RTNN), a site in the National Nanotechnology Coordinated Infrastructure (NNCI).

Appendix A. Supplementary data

Supplementary data to this article can be found online at https://do i.org/10.1016/j.jssc.2021.122419.

References

- [1] B.L. Musico, D. Gilbert, T.Z. Ward, K. Page, E. George, J. Yan, D. Mandrus, V. Keppens, The emergent field of high entropy oxides: design, prospects, challenges, and opportunities for tailoring material properties, Apl. Mater. 8 (1–8) (2020) 040912
- [2] R. Cava, Oxide superconductors, J. Am. Ceram. Soc. 83 (2000) 5-28.
- [3] K.N.D.K. Muhsen, R.A.M. Osman, M.S. Idris, The effects of Ca, Zr, and Sn substitutions into a ternary system of BaTiO₃-BaSnO₃-BaZrO₃ towards its dielectric and piezoelectric properties: a review, J. Mater. Sci. Mater. Electron. (2020).
- [4] B. Yan, M. Jansen, C. Felser, A large-energy-gap oxide topological insulator based on the superconductor BaBiO₃, Nat. Phys. 9 (2013) 709–711.
- [5] N. McLamb, P.P. Sahoo, L. Fuoco, P.A. Maggard, Flux growth of single-crystal Na₂Ta₄O₁₁ particles and their photocatalytic hydrogen production, Cryst. Growth Des. 13 (2013) 2322–2326.
- [6] S.M. Schmuecker, D. Clouser, T.J. Kraus, B.M. Leonard, Synthesis of metastable chromium carbide nanomaterials and their electrocatalytic activity for the hydrogen evolution reaction, Dalton Trans. 46 (2017) 13524–13530.
- [7] J. Boltersdorf, P.A. Maggard, Silver exchange of layered metal oxides and their photocatalytic activities, ACS Catal. 3 (2013) 2547–2555.
- [8] S. O'Donnell, C. Chung, A. Carbone, R. Broughton, J.L. Jones, P.A. Maggard, Pushing the limits of metastability in semiconducting perovskite oxides for visiblelight-driven water oxidation, Chem. Mater. 32 (7) (2020) 3054–3064.
- [9] J. Gardner, A. Thakre, A. Kumar, J.F. Scott, Tin titanate-the hunt for a new ferroelectric perovskite, Rep. Prog. Phys. 82 (9) (2019) 1–14, 092501.

- [10] E. Sawaguchi, Ferrolectricity versus antiferroelectricity in the solid solutions of PbZrO₃ and PbTiO₃, J. Phys. Soc. Jpn. 8 (5) (1953) 615–629.
- [11] M.A. Knyazeva, D.A. Andronikova, G.A. Lityagin, I.A. Bronwald, P. Paraskevas, A. Majchrowski, K. Roleder, A.V. Filimonov, R.G. Burkovsky, Phase transitions in lead hafnate under high pressure, Phys. Solid State 61 (10) (2019) 1806–1812.
- [12] A. Walsh, D.J. Payne, R.G. Egdell, G.W. Watson, Stereochemistry of post-transition metal oxides: revision of the classic lone pair model, Chem. Soc. Rev. 40 (2011) 4455–4463.
- [13] C.M. Campo, J.E. Rodriguez, A.E. Ramirez, Thermal behavior of romarchite phase SnO in different atmospheres: a hypothesis about the phase transformation, Heliyon 2 (5) (2016) e00112.
- [14] F. Bortolani, R.A. Dorey, Molten salt synthesis of PZT powder for direct write inks, J. Eur. Ceram. Soc. 30 (2010) 2073–2079.
- [15] S.S. Chandratreya, R.M. Fulrath, J.A. Pask, Reaction mechanisms in the formation of PZT solid solutions, J. Am. Ceram. Soc. 64 (7) (1981) 422–425.
- [16] K.C. Pitike, W.D. Parker, L. Louis, S.M. Nakhmanson, First-principles studies of lonepair-induced distortions in epitaxial phases of perovskite SnTiO₃ and PbTiO₃, Phys. Rev. B 91 (2015), 035112.
- [17] L. Diehl, S. Bette, F. Pielnhofer, S. Betzler, I. Moudrakovskit, G.A. Ozin, R. Dinnebier, B.V. Lotsch, Structure-directing lone pairs: synthesis and structural characterization of SnTiO₃, Chem. Mater. 30 (24) (2018) 8932–8938.
- [18] S. Kirklin, J.E. Saal, B. Meredig, A. Thompson, J.W. Doak, M. Aykol, S. Rühl, C. Wolverton, The open Quantum materials Database (OQMD): assessing the accuracy of DFT formation energies, Npj. Compu. Mater. 1 (September) (2015).
- [19] J.E. Saal, S. Kirklin, M. Aykol, B. Meredig, C. Wolverton, Materials design and discovery with high-throughput density functional theory: the open Quantum materials Database (OQMD), JOM (J. Occup. Med.) 65 (11) (2013) 1501–1509.
- [20] S. O'Donnell, A. Hamilton, P.A. Maggard, Fast flux reaction approach for the preparation of Sn₂TiO₄: tuning particle sizes and photocatalytic properties, J. Electrochem. Soc. 166 (5) (2019) 3084–3090.
- [21] J. Boltersdorf, I. Sullivan, T.L. Shelton, Z. Wu, M. Gray, B. Zoellner, F.E. Osterloh, P.A. Maggard, Flux synthesis, optical, and photocatalytic properties of n-type Sn₂TiO₄: hydrogen and oxygen evolution under visible light, Chem. Mater. 28 (24) (2016) 8876–8889.
- [22] W. Sun, S.T. Dacek, S.P. Ong, G. Hautier, A. Jain, W.D. Richards, A.C. Gamst, K.A. Persson, G. Ceder, The thermodynamic scale of inorganic crystalline metastability, Sci. Adv. 2 (2016) 1600225.
- [23] M. Aykol, S.S. Dwaraknath, W. Sun, K.A. Persson, Thermodynamic limit for synthesis of metastable inorganic materials, Sci. Adv. 4 (2018), 0148.
- [24] Q. Mahmood, B. Ul Haq, M. Yaseen, S.M. Ramay, M.G.B. Ashiq, A. Mahmood, The first-principle study of mechanical, optical and thermoelectric properties of SnZrO₃ and SnHfO₃ for renewable energy applications, Solid State Commun. 292 (2019) 17–23.

- [25] D. Chenine, Z. Aziz, Theoretical investigation of structural, elastic and electronic properties of SnHfO₃ compound: Ab initio calculations, in: Proceedings of the Third International Symposium on Materials and Sustainable Development, 2018, nn. 75–80
- [26] J. Wang, Mixed valence tin oxides as Novel van der Waals materials: theoretical predictions and potential applications, Adv. Energy Mater. 6 (1–11) (2016) 1501190.
- [27] A. Seko, A. Togo, F. Oba, I. Tanaka, Structure and stability of a homologous series of tin oxides, Phys. Rev. Lett. 100 (1–4) (2008), 045702.
- [28] B.H. Toby, R.B. Von Dreele, GSAS-II: the genesis of a modern open-source all purpose crystallography software package, J. Appl. Crystallogr. 46 (2) (2013) 544–549.
- [29] G. Kreese, J. Hafner, Efficiency of Ab initio total energy calculations for metals and semiconductors using a plane-wave basis set, Comput. Mater. Sci. 6 (1996) 6–15.
- [30] G. Kreese, J. Furthmuller, Efficient iterative schemes for Ab initio total-energy calculations using a plane-wave basis set, Phys. Rev. B 6 (1996) 11169–11186.
- [31] J.P. Perdew, L. Burke, M. Ernzerhof, Generalized gradient approximation made simple, Phys. Rev. Lett. 77 (1996) 3865–3868.
- [32] G. Hautier, S. Ping Ong, A. Jain, C.J. Moore, G. Ceder, Accuracy of density functional theory in predicting formation energies of ternary oxides from binary oxides and its implication on phase stability, Phys. Rev. B 85 (2012) 155208.
- [33] A. Benisek, E. Dachs, The accuracy of standard enthalpies and entropies for phases of petrological interest derived from density-functional calculations, Contrib. Mineral. Petrol. 173 (90) (2018) 1–11.
- [34] K. Momma, F. Izumi, VESTA 3 for three-dimensional visualization of crystal, volumetric and morphology data, J. Appl. Crystallogr. 44 (2011) 1272–1276.
- [35] A. Dias, V.S.T. Ciminelli, Electroceramic materials of tailored phase and morphology by hydrothermal technology, Chem. Mater. 15 (2003) 1344–1352.
- [36] S. Ullah, T. Iqbal, G. Rehman, I. Ahmad, Electronic and optical properties of group IIA-IVB cubic perovskite oxides: improved TB-mBJ study, Chem. Phys. Lett. 757 (2020) 137887.
- [37] S. Upadhyay, O. Parkash, Preparation and Characterization of barium stannate BaSnO3, J. Mater. Sci. Lett. 16 (1997) 1330–1332.
- [38] H. Giefers, F. Porsch, G. Wortmann, Kinetics of the disproportionation of SnO, Solid State Ionics 1–2 (176) (2005) 199–207.
- [39] M.S. Moreno, G. Punte, G. Rigotti, R.C. Mercader, A.D. Weisz, M.A. Blesa, Kinetic study of the disproportionation of tin monoxide, Solid State Ionics 1–2 (144) (2001) 81, 96
- [40] J. Tateno, An empirical relation on the melting temperature of some ionic crystals, Solid State Commun. 10 (1972) 61–62.
- [41] S.-N. Luo, Vibrational density of states and Lindemann melting law, J. Chem. Phys. 122 (1–5) (2005) 194709.